



HAL
open science

Proton acceleration by collisionless shocks using a supersonic H₂ gas-jet target and high-power infrared laser pulses

P. Puyuelo-Valdes, J. Henares, F. Hannachi, T. Ceccotti, J. Domange, M. Ehret, E. d'Humieres, L. Lancia, Jean-Raphaël Marquès, X. Ribeyre, et al.

► To cite this version:

P. Puyuelo-Valdes, J. Henares, F. Hannachi, T. Ceccotti, J. Domange, et al.. Proton acceleration by collisionless shocks using a supersonic H₂ gas-jet target and high-power infrared laser pulses. *Physics of Plasmas*, 2019, 26 (12), pp.123109. 10.1063/1.5116337 . hal-02418729

HAL Id: hal-02418729


<https://hal.sorbonne-universite.fr/hal-02418729>

Submitted on 8 Dec 2020

HAL is a multi-disciplinary open access archive for the deposit and dissemination of scientific research documents, whether they are published or not. The documents may come from teaching and research institutions in France or abroad, or from public or private research centers.

L'archive ouverte pluridisciplinaire **HAL**, est destinée au dépôt et à la diffusion de documents scientifiques de niveau recherche, publiés ou non, émanant des établissements d'enseignement et de recherche français ou étrangers, des laboratoires publics ou privés.

AUTHOR QUERY FORM

	<p>Journal: Phys. Plasmas</p> <p>Article Number: POP19-AR-58116</p>	<p>Please provide your responses and any corrections by annotating this PDF and uploading it to AIP's eProof website as detailed in the Welcome email.</p>
---	--	--

Dear Author,

Below are the queries associated with your article; please answer all of these queries before sending the proof back to AIP.

Article checklist: In order to ensure greater accuracy, please check the following and make all necessary corrections before returning your proof.

1. Is the title of your article accurate and spelled correctly?
2. Please check affiliations including spelling, completeness, and correct linking to authors.
3. Did you remember to include acknowledgment of funding, if required, and is it accurate?

Location in article	Query / Remark: click on the Q link to navigate to the appropriate spot in the proof. There, insert your comments as a PDF annotation.
AQ1	Please check that the author names are in the proper order and spelled correctly. Also, please ensure that each author's given and surnames have been correctly identified (given names are highlighted in red and surnames appear in blue).
AQ2	Please define PSL at first occurrence.
AQ3	In Refs. 3-5, and 24 please provide a brief description of the information available at the website. For example, "See XX for information about XXX."
AQ4	Please check and confirm the edits made in Refs. 11 and 20.
AQ5	Please provide volume and page number for Ref. 12.
AQ6	Please specify which section or subsection "in the following section" refers to here.
AQ7	<p>We were unable to locate a digital object identifier (doi) for Ref(s). 6, 7, 15, 21, 31. Please verify and correct author names and journal details (journal title, volume number, page number, and year) as needed and provide the doi. If a doi is not available, no other information is needed from you. For additional information on doi's, please select this link: http://www.doi.org/.</p> <p>Please confirm ORCID's are accurate. If you wish to add an ORCID for any author that does not have one, you may do so now. For more information on ORCID, see https://orcid.org/.</p> <p>P. Puyuelo-Valdes-</p> <p>J. L. Henares - 0000-0001-8990-4839</p> <p>F. Hannachi-</p> <p>T. Ceccotti-</p> <p>J. Domange-</p> <p>M. Ehret - 0000-0002-7671-6246</p>

E. d'Humieres-

L. Lancia - 0000-0001-7501-3648

J.-R. Marquès-

X. Ribeyre - 0000-0002-9823-2744

J. J. Santos - 0000-0002-4737-8559

V. Tikhonchuk - 0000-0001-7532-5879

M. Tarisien - 0000-0002-6292-2241

Please check and confirm the Funder(s) and Grant Reference Number(s) provided with your submission:

Agence Nationale de la Recherche, Award/Contract Number 17-CE30-0026-02

Agence Nationale de la Recherche, Award/Contract Number 10-IDEX-03-02

Centre National de la Recherche Scientifique, Award/Contract Number ALP-IONS

Compute Canada, Award/Contract Number pve-323-ac

Conseil Régional Aquitaine, Award/Contract Number POPRA

Please add any additional funding sources not stated above:

Thank you for your assistance.

Proton acceleration by collisionless shocks using a supersonic H₂ gas-jet target and high-power infrared laser pulses

Cite as: Phys. Plasmas **26**, 000000 (2019); doi: 10.1063/1.5116337

Submitted: 25 June 2019 · Accepted: 22 November 2019 ·

Published Online: 0 Month 0000



View Online



Export Citation



CrossMark

P. Puyuelo-Valdes,^{1,2} J. L. Henares,¹ F. Hannachi,¹ T. Ceccotti,³ J. Domange,¹ M. Ehret,^{4,5} E. d'Humieres,⁴ L. Lancia,⁶ J.-R. Marquès,⁶ X. Ribeyre,⁴ J. J. Santos,⁴ V. Tikhonchuk,⁴ and M. Tarisien¹

AFFILIATIONS

¹CENBG, CNRS-IN2P3, Université de Bordeaux, 33175 Gradignan Cedex, France

²INRS-EMT, 1650 Blvd. Lionel-Boulet, Varennes, Quebec J3X 1P7, Canada

³LIDYL, CNRS, CEA, Université de Paris-Saclay, 91191 Gif-Sur-Yvette Cedex, France

⁴CELIA, CNRS, CEA, Université de Bordeaux, UMR 5107, 33400 Talence, France

⁵Institut für Kernphysik, Technische Universität Darmstadt, 64289 Darmstadt, Germany

⁶LULI, Ecole Polytechnique, 91128 Palaiseau Cedex, France

ABSTRACT

For most laser-driven ion acceleration applications, a well-characterized intense ion beam with a low divergence and a controllable energy spectrum produced at a high repetition rate is needed. Gas-jet targets have given promising results in simulations, and they have several technical advantages for high-repetition-rate lasers. In this work, we report on proton acceleration to energies up to 6 MeV using a supersonic H₂ gas-jet target at the LULI PICO2000 laser facility. The experimental results are compared with the plasma hydrodynamics and the particle-in-cell simulations to identify the acceleration mechanisms at play.

Published under license by AIP Publishing. <https://doi.org/10.1063/1.5116337>

I. INTRODUCTION

Laser-driven ion acceleration techniques are under rapid development due to a large potential range of applications.^{1,2} For most of them, a well-characterized intense ion beam with a well-defined energy distribution is needed. This requires the quantitative optimization of the laser-matter interaction parameters. Numerical simulations help to identify the most appropriate parameters related to the explored acceleration mechanism. Nevertheless, the experimental phase of such an optimization work is quite time consuming. Now, with the new generation of high-power laser facilities operating at a high repetition rate (as APOLLON in France,³ ELI pillars in Europe,⁴ or VEGA in Spain⁵), this is more accessible.

Solid targets are used for ion acceleration in most experiments for their high density, the simplicity of fabrication, and alignment. However, the replacement and the realignment of the target are mandatory after each laser shot, and the interaction generates debris that damages the optical elements. A large effort has been made to develop fast-moving, high-repetition-rate target holders which contain several solid targets. Even if considerable improvement has been achieved, avoiding debris deposition and target replacement after several shots

still represent a challenge. A particular kind of solid target, which can be regenerated *in situ*, is cryogenic ribbons.^{6,7} These could be clean sources of protons or deuterons, free of contaminants and operating at a high repetition rate. For instance, a flux of 10⁹ protons/MeV/sr with a maximum energy of 18 MeV was reported at the 150 TW ultrashort pulse laser Draco, HZDR with a planar (20 × 2 μm²) cryogenic hydrogen jet.⁷ The acceleration regime was Target Normal Sheath Acceleration (TNSA) producing broad energy distributions.⁸

Another option consists of using liquid targets as water droplets^{9–12} or liquid crystal films.¹³ In 2018, Hilz *et al.*¹² observed proton bunches with energies between 20 and 40 MeV using the PHELIX PW laser at GSI delivering 500 fs pulses with an energy of 150 J. The acceleration mechanism reported is the Coulomb repulsion.

Near-critical-density gas-jet targets are an interesting alternative for the acceleration of different ion species as they can be used at a high repetition rate and are debris-free. Moreover, a strong electrostatic field inducing a more efficient ion acceleration than TNSA can be produced in near-critical-density plasmas. This acceleration scheme involving collisionless shock waves had been first introduced by Silva *et al.*¹⁴ for overdense plasma targets and expanded by d'Humières

64 *et al.*¹⁵ to underdense ones. In near-critical-density plasmas using a
 65 CO₂ laser, Haberberger *et al.*¹⁶ demonstrated that the laser-driven col-
 66 lisionless shocks can accelerate proton beams to 20 MeV with a narrow
 67 energy spread of about 1% and a low emittance.

68 Gas jets are promising targets, and nozzles capable of generating
 69 the required plasma densities have to be designed. Several results were
 70 published using CO₂ lasers, which correspond to a critical density (n_c)
 71 of 10^{19} cm⁻³.¹⁶⁻¹⁸ However, the presently developed high-energy
 72 near-infrared lasers correspond to $n_c \sim 10^{21}$ cm⁻³, which are still very
 73 challenging to produce with supersonic gas jets. Only a few experi-
 74 ments have been performed so far. In 2013, Sylla *et al.*¹⁹ carried out
 75 one with the “Salle Jaune” laser at LOA using a submillimetric super-
 76 sonic 0.95 n_c density helium jet from a conical nozzle. They observed
 77 He⁺ ions with energies of up to 250 keV in the transverse direction. In
 78 2017, Chen *et al.*²⁰ at the TITAN laser facility at LLNL used a super-
 79 sonic 2.5 n_c density hydrogen jet from a rectangular nozzle and
 80 observed protons with energies of up to 0.8 MeV in the longitudinal
 81 direction.

82 We have developed a series of near-critical gas-jet targets for
 83 1 μ m wavelength lasers. Computational fluid dynamics (CFD) simu-
 84 lations have been performed to design the corresponding supersonic
 85 gas-jet nozzles. The target density profiles were measured by inter-
 86 ferometry and compared with the simulation results. More details have
 87 been published in Refs. 21 and 22.

88 In this paper, we report on the proton acceleration of up to
 89 6 MeV in a high-density H₂ gas jet at the PICO2000 laser facility at
 90 LULI. Hereinafter, the setup and the experimental results are pre-
 91 sented. The latter are compared with the hydrodynamics and the
 92 Particle-in-Cell (PIC) simulations.

93 **II. EXPERIMENTAL SETUP**

94 A 1000 bar Haskel gas booster coupled to a Clark-Cooper sole-
 95 noid valve and a convergent-divergent conical nozzle (a 100 μ m
 96 diameter, a 1 mm length, and a 240 μ m exit diameter) were employed
 97 to generate supersonic H₂ gas-jet targets. The PICO2000 laser beam at
 98 a wavelength $\lambda = 1053$ nm, a 1 ps pulse duration, and a 60 J energy
 99 was focused on the gas jet, at 400 μ m from the nozzle exit, in a 12 μ m
 100 Full Width at Half Maximum (FWHM) diameter spot providing an
 101 intensity of 5×10^{19} W/cm². The Amplified Spontaneous Emission
 102 (ASE) duration was of the order of 250 ps, with its level $\sim 10^6$ below
 103 the picosecond pulse maximum.

104 The gas-jet target alignment was achieved using the bottom and
 105 the side views placed in the chamber. Four Thomson Parabolas (TP)
 106 with their respective Imaging Plate detectors (IP) were used to detect
 107 and resolve the accelerated ions in charge and energy. They were
 108 placed at 0°, 30°, 70°, and 80° with respect to the laser axis (Fig. 1).
 109 They were shielded by lead walls for a signal-to-background ratio
 110 improvement and were equipped with pinholes at their entrances for a
 111 better energy resolution. BAS-TR and BAS-MS IPs for the Fuji
 112 Photo-Film Co. Ltd., were used and analyzed using a FUJIFILM FLA-
 113 700 reader. The IP response function to protons has been taken from
 114 Ref. 23. All TPs have been calibrated in energy at the AIFIRA accelera-
 115 tor facility at CENBG,²⁴ in the energy range from 500 keV to 3.5 MeV.
 116 The uncertainties in the energy value and in the number of protons/
 117 MeV/sr (N_p /MeV/sr) were calculated assuming that all variables (solid
 118 angle, response function, number of PSL, energy calibration) are statisti-
 119 cally independent and summing their variances. The energy is

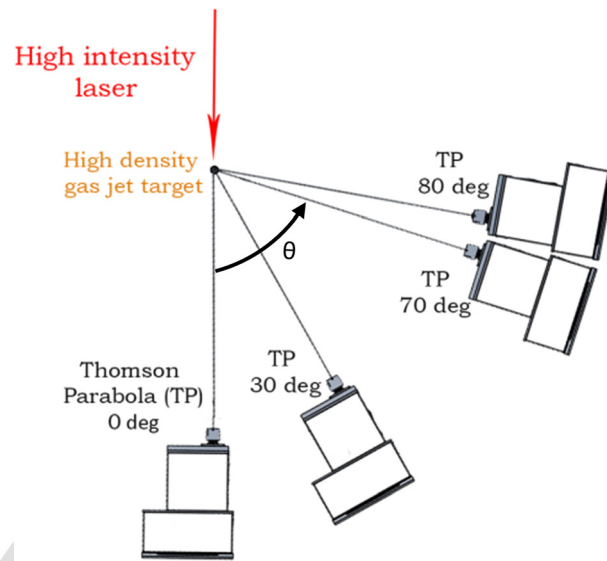


FIG. 1. Experimental setup at the LULI facility: PICO2000 high-power laser was incident on a high-density H₂ gas jet. Four Thomson Parabolas (TPs) equipped with Imaging Plate detectors (IPs) were placed at 0°, 30°, 70°, and 80° with respect to the laser axis.

measured with an accuracy of about 3%. The accuracy of N_p /MeV/sr 120
 is about 50% at low energies and about 20% at high energies. 121

The BAS-MS films have a 9 μ m protective layer which stops pro- 122
 tons with energies lower than 600 keV, while the BAS-TR films are 123
 layer-free. Examples of the proton spectra in Fig. 2 show about a one 124
 order of magnitude difference in their background levels. The BAS-TR 125
 IPs display a background of $(1.9 \times 10^9 \pm 1.4 \times 10^9)$ protons/MeV/sr, 126
 while for the BAS-MS IPs, it is $(0.25 \times 10^9 \pm 0.22 \times 10^9)$ protons/ 127
 MeV/sr. This is probably due to their different sensibility to UV light. 128
 Therefore, we chose to employ the BAS-MS IPs despite the loss of the 129
 lowest part of the energy distribution. 130

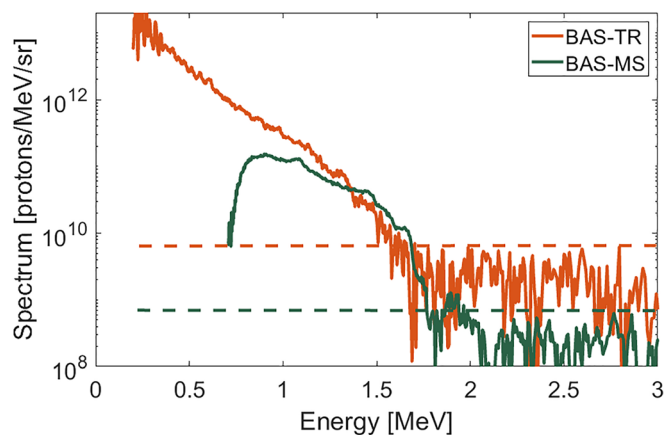


FIG. 2. Proton energy spectra recorded at 30° from two analog shots using both types of IPs. The one in orange is from a BAS-TR IP, while the green one is from the BAS-MS IP. Dashed lines indicate the detection limit corresponding to the mean value of the background level plus two times its variance.

AQ2

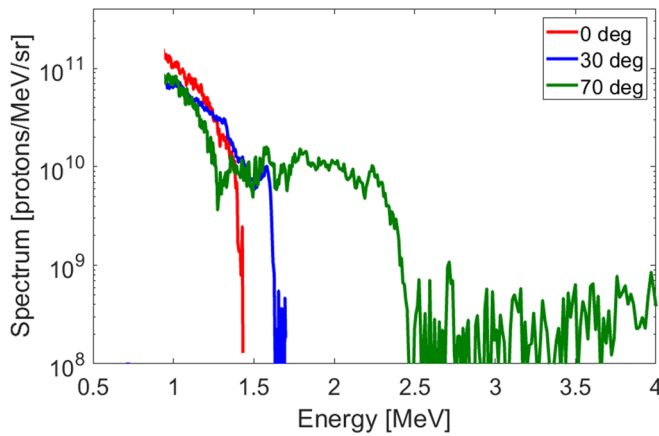


FIG. 3. Proton energy spectra at 0° (red), 30° (blue), and 70° (green) obtained with the laser focused at the center of the jet.

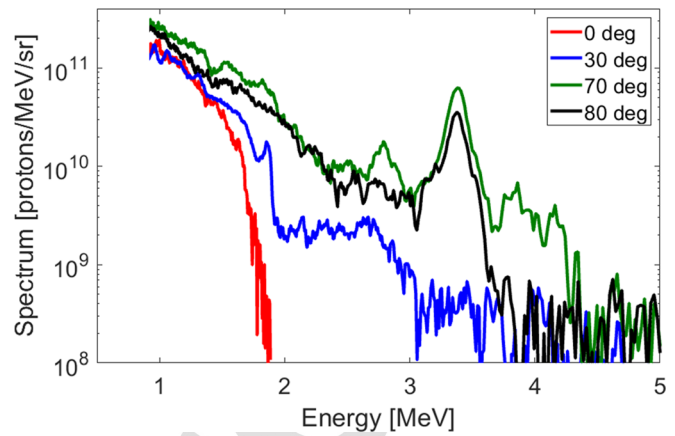


FIG. 5. Proton energy spectra at 0° (red), 30° (blue), 70° (green), and 80° (black) obtained with the laser focused at the rising slope of the jet density profile.

131 III. EXPERIMENTAL RESULTS

132 Figure 3 shows the typical spectra obtained with the laser focused
 133 at the center of the gas jet. About 10^{11} protons/MeV/sr in a continuous
 134 energy distribution of up to 1.5 MeV are observed in the longitudinal
 135 direction (0°). A similar flux in that same energy range is also observed
 136 in the other directions (30° and 70°). Furthermore, a second structure
 137 of up to 2.5 MeV is observed in the transverse direction containing
 138 10^{10} protons/MeV/sr. Unfortunately, the TP at 80° was not in place
 139 on these first shots.

140 The proton maximum energy was increased when the laser was
 141 focused at the rising slope of the gas-jet density profile, at about 70 μm
 142 from its center. Figure 4 shows the typical spectra recorded in this con-
 143 figuration. Besides the structures already presented in Fig. 3, an addi-
 144 tional peak at 2.3 MeV is observed at 0°. A high proton flux (about
 145 10^{11} protons/MeV/sr) in the energy range of up to 3 MeV is also
 146 observed in the transverse direction.

147 It is worth noting that the angular position and the energy of the
 148 peaked structure at 0° in Fig. 4 are highly dependent on the laser and

the target parameters. Small variations of these (for example, lower
 149 maximum density of the gas jet and laser fluctuations) can shift the
 150 peak to the transverse directions (70° and 80°) and to higher energies
 151 (3.3 MeV), as seen in Fig. 5. In addition, a plateau structure in the
 152 energy range of 2–3 MeV is observed at 30°. Similar features in the
 153 transverse direction can be seen in Figs. 3 and 4.

154 The effect of ASE on the proton spectra was also studied. The
 155 level of ASE is controlled by the variation of the timing of two Pockels
 156 cells which isolate the main short picosecond pulse from the amplified
 157 nanosecond background. Figure 6 presents the proton energy distribu-
 158 tion when the ASE level is reduced at the minimum achievable. The
 159 spectra display more complex structures. The proton flux at 80° is
 160 smaller than in previous shots, while the maximum energy at 0° is
 161 higher. Three particular features can be seen on the spectrum in the
 162 longitudinal direction. The proton flux drops from 10^{11} to 10^9 in
 163 the energy range between 0.5 and 2 MeV. Then, it increases up to 10^{10}
 164 between 1.7 and 3 MeV, and a third peak with a flux of 5×10^9 is
 165

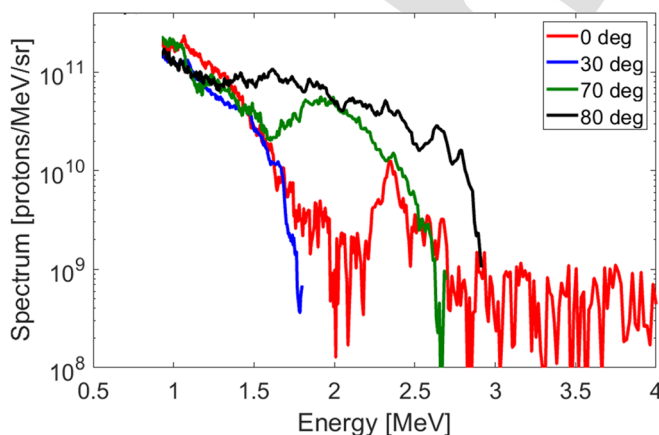


FIG. 4. Proton energy spectra at 0° (red), 30° (blue), 70° (green), and 80° (black) obtained with the laser focused at the rising slope of the jet density profile.

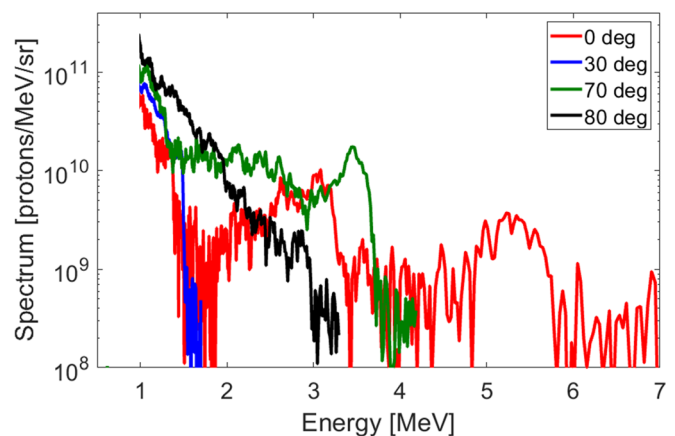


FIG. 6. Proton energy spectra at 0° (red), 30° (blue), 70° (green), and 80° (black) obtained with the laser focused at the rising slope of the jet density profile. The ASE level was reduced for this shot.

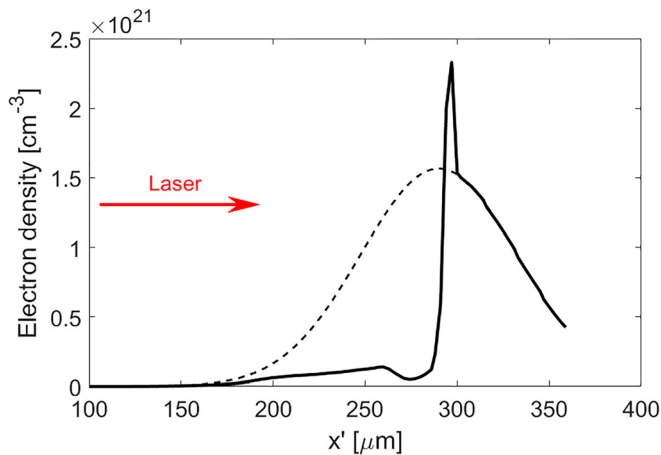


FIG. 7. Dashed line: the initial density profile of the gas jet based on measurements. Solid line: the density profile calculated with the FLASH code taking into account the laser ASE and used as input in the PIC simulations.

166 observed in the range of 4.3–5.3 MeV. Another peak at the energy of
167 3.4 MeV can also be seen at 70°.

168 IV. HYDRODYNAMICS AND PIC SIMULATIONS

169 Numerical simulations with the two-dimensional Particle-in-
170 Cell (2D PIC) code, PICLS,²⁵ were used for the interpretation of the
171 measured proton spectra. The PICO2000 laser parameters at the
172 normal incidence and the s-polarization were used as inputs. The
173 temporal and the spatial laser intensity profiles are described by the
174 truncated Gaussian functions. The laser temporal pulse is truncated
175 at 2 ps. The pulse is injected at the left side of the simulation box
176 ($600 \times 160 \mu\text{m}^2$) at a time $t = 0$. Assuming that the high-intensity
177 laser pulse fully ionizes the gas, the target is described as a 380 μm
178 length plasma of electrons and protons. The mesh size is 80 nm,

and 15 particles of each species were used in each cell. Physical processes
are simulated during 3.6 ps with a time step of 0.267 fs. Absorbing
boundary conditions for the fields and the particles are applied.

The plasma density profile in the PIC simulations accounts for the
interaction of the laser ASE with the initial gas density profile. This
has been modeled with the 3D hydrodynamic code FLASH.²⁶ In this
simulation, the gas jet is contained in a cylinder of a 200 μm diameter
center on the maximum of its radial density profile. The dimensions
of the simulation box are $560 \times 120 \times 120 \mu\text{m}^3$, and the center of the
cylinder is at $x' = 290 \mu\text{m}$ from the laser arrival side. The prepulse
radial distribution is the same as the main pulse one with the maxi-
mum intensity reduced by a factor of 10^6 (corresponding to the cut of
1 ns on the Pockels cell timing).

For example, Fig. 7 shows the initial Gaussian density profile of
the gas jet (dashed line) and the calculated density profile (solid line)
in the laser propagation direction 240 ps after the start of the simu-
lation, which is of the order of the ASE duration in the experiment. The
left part of the initial density profile is dramatically modified, and a
shock is formed with a peak of approximately twice the original den-
sity. The exact location of the peak and its magnitude depend on the
ASE duration which has not been precisely measured in this experi-
ment. The consequences of a different density profile are discussed at
the end of Sec. IV. A low-density plasma remains in the left part of
the density profile.

In Fig. 8, a 2D slice of the 3D electron density calculated with the
code FLASH at $t = 240$ ps is represented. It shows that the laser pen-
etrates up to the critical density and produces a density channel in the
gas jet. It is worth noting that the density on the y axis is constant over
the focal spot diameter of 12 μm ; therefore a constant y density is
introduced in the PIC simulations.

The plasma density profile used as input in the PIC simulations
is shown in Fig. 9(1). To simplify the calculations, the plasma den-
sity on the x axis is assumed to be constant ($\sim 10^{19} \text{cm}^{-3}$) for $x < 185 \mu\text{m}$
and increases to the maximum value of $\sim 2.4 \times 10^{21} \text{cm}^{-3}$ over a

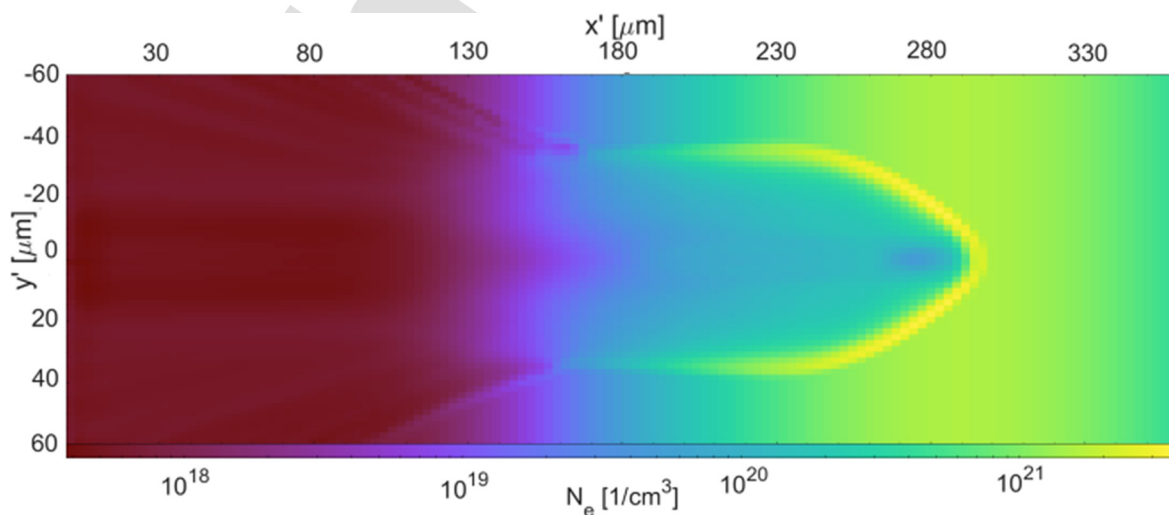


FIG. 8. 2D slice of the 3D electron density in the FLASH simulation at $t = 240$ ps, the time of the main pulse arrival.

214 distance of $5 \mu\text{m}$, ($x = 190 \mu\text{m}$ in the PIC simulation corresponds to
 215 $x' = 297 \mu\text{m}$ in FLASH simulations since the left edge of the plasma
 216 was defined as $x = 0$ in the PIC simulations). For $x > 200 \mu\text{m}$, the initial
 217 Gaussian profile has been used without any modification. Sharp
 218 plasma borders generate artifacts in the PIC simulation. Since real gas
 219 edges are not sharp, a slope of 15% of the plasma length was used at
 220 each border of the plasma in order to minimize this effect. Particles
 221 accelerated in these parts are not considered in the analysis. The initial
 222 plasma temperature is set to zero.

223 The PIC simulation results are presented in Fig. 9 for the particle
 224 energy density at four consecutive instants and are discussed in detail
 225 in the following sections:

- 226 • $t = 1 \text{ ps}$, laser penetrates to the density of $\sim 10^{19} \text{ cm}^{-3}$ [Fig. 9(a),
 227 Sec. IV A];
- 228 • $t = 1.8 \text{ ps}$, laser attains the maximum plasma density of $> n_c$ [Fig.
 229 9(b), Sec. IV B];
- 230 • $t = 2.3 \text{ ps}$, soon after [Fig. 9(c), Sec. IV B]; and
- 231 • $t = 3.6 \text{ ps}$, at the end of the simulation [Fig. 9(d), Sec. IV C].

A. Laser interaction with the underdense plasma 232

233 As the laser penetrates in the underdense plasma, the electrons
 234 are heated and expelled radially by the laser ponderomotive force. A
 235 channel is formed, and the protons are accelerated radially by the
 236 charge separation electric field. At $t = 1 \text{ ps}$, self-focusing and self-
 237 channeling of the laser pulse are observed. These are due to the elec-
 238 tron expulsion by the laser ponderomotive force and the relativistic
 239 increase in the electron mass. As the laser pulse power is larger than
 240 the critical power of self-focusing, multiple filaments are formed
 241 [Fig. 9(a)].

242 The proton phase spaces at $t = 1 \text{ ps}$ are shown in Fig. 10. At first,
 243 the protons are accelerated at the plasma edge $x = 0$. However, the
 244 radial acceleration dominates: the transverse momentum, p_y , displayed
 245 in Fig. 10(b) is much larger than the longitudinal one, p_x , shown in
 246 Fig. 10(a).

247 The proton angular energy distribution in the forward ($p_x \geq 0$)
 248 direction is displayed in Fig. 11. Most of the protons are accelerated in
 249 the transverse direction during the laser channeling in the underdense

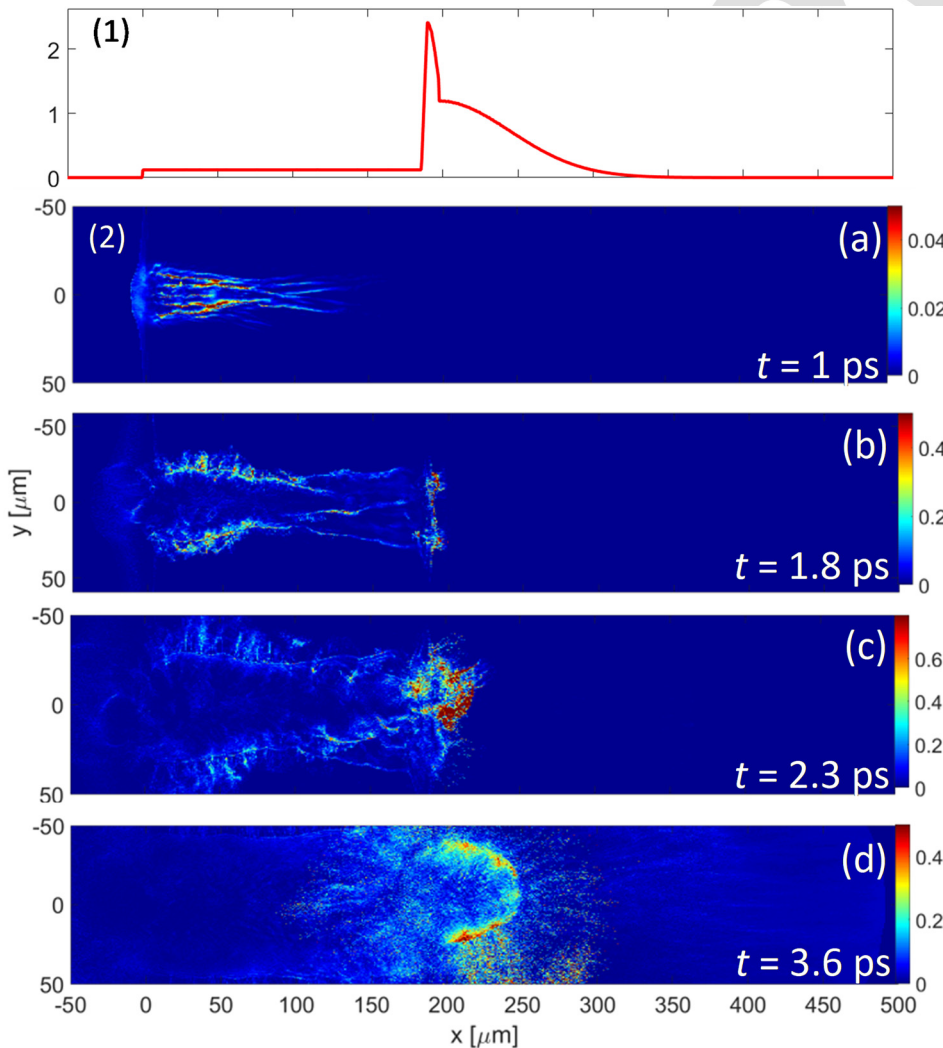


FIG. 9. (1) Proton density profile (in n_c units) at $t = 0 \text{ ps}$. (2) Evolution of the proton energy density (in relativistic units, $n_c m_e c^2$) in the PIC simulation: (a) $t = 1 \text{ ps}$, (b) 1.8 ps , (c) 2.3 ps , and (d) 3.6 ps .

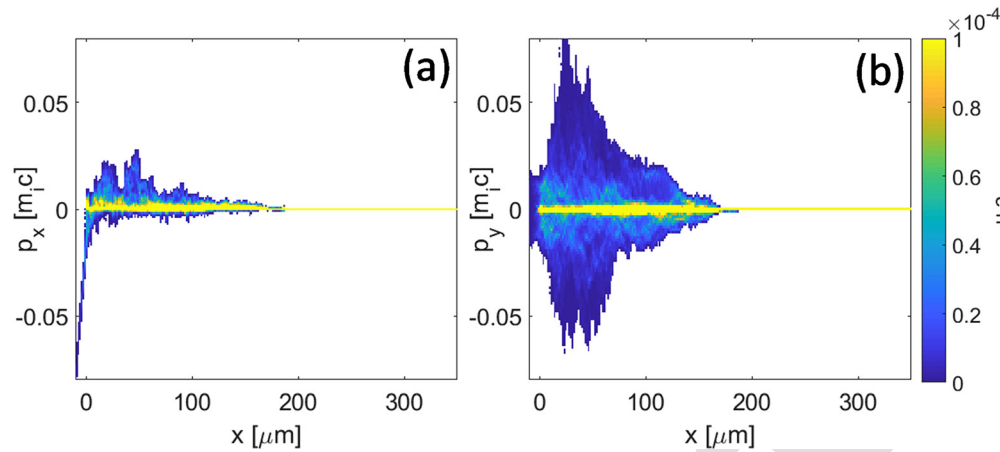


FIG. 10. Proton phase space histogram at time $t = 1$ ps: (a) longitudinal and (b) transverse momenta as a function of the longitudinal coordinate.

250 plasma. This particular feature of gas-jet experiments has been
251 reported even in the case of helium acceleration.^{19,27–31}

252 **B. Laser interaction with the overcritical plasma**

253 At $t = 1.8$ ps when the laser pulse reaches the maximum target
254 density, one observes more complex interaction processes. Figure
255 12(a) evidence a collisionless shock formed at $x = 185 \mu\text{m}$ which
256 accelerates protons both forward and backward (see the red box).
257 This shock is the result of the laser intensity profile steepening: the
258 increased radiation pressure pushes the plasma density forward,
259 and the so-called hole boring process takes place [Fig. 9(b)].³² The
260 proton acceleration in the shock is essentially longitudinal.
261 However, there is a small component in the transverse direction as
262 shown in Fig. 12(b).

The angular energy distribution of protons accelerated in the forward direction is presented in Fig. 13(a). Similarly to the previous instant shown in Fig. 11, the majority of protons are accelerated in the transverse direction. However, there is a small fraction of protons that are accelerated in the longitudinal direction. Figure 13(b) confirms their origin: the angular energy distribution of the protons accelerated in the interval $x = 185 \mu\text{m}$ and $x = 210 \mu\text{m}$ presents a forward energetic component as shown in the phase space in the red square in Fig. 12.

In the hole boring process, the details of the shock instability strongly depend on the interaction conditions: the initial plasma temperature and the density profile.³³ Figure 14(b) shows the shock-accelerated protons in the direction of 50° with energies of up to 25 MeV higher than those accelerated by laser channeling (up to 15 MeV). Furthermore, in Fig. 15, which represents the spatial distribution of the period-averaged electromagnetic laser energy at $t = 2.3$ ps, one can see that most part of the laser is reflected at $x = 185 \mu\text{m}$, except for a small part in which the direction is also bent.

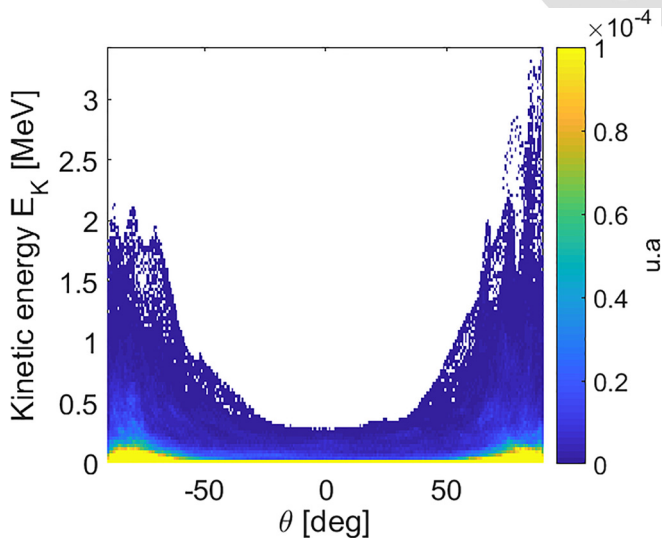


FIG. 11. Angular energy distribution of forward ($p_x \geq 0$) accelerated protons at $t = 1$ ps.

280 **C. Longer times: Laser beam collapse**

281 The laser beam, which has deviated from its initial propagation
282 direction, cannot penetrate further in the plasma. For $t > 2.5$ ps in the
283 simulation [Fig. 9(d)], we observe the laser beam collapse as previously
284 reported in Ref. 19.

285 Figure 16 shows the simulated proton energy distribution in the
286 directions where TPs were set in the experiment within 10° wide angular
287 windows. The spectra at all angles are continuously decreasing,
288 while at the angles of 0° and 30° , there is a second plateau structure at
289 a high energy. The latter is due to the particles accelerated by the collisionless
290 shock, already analyzed in Sec. IV B and observed in Fig. 14.

291 **D. Discussion**

292 The goal of these simulations was to interpret the measured proton
293 spectra and understand their origins. Figure 16 allows to compare the
294 simulated energy distributions with the measured ones (Sec. III).
295 However, it is worth noting that the maximum energies and the higher
296 particle fluxes are found at 50° in the simulation (Fig. 14).

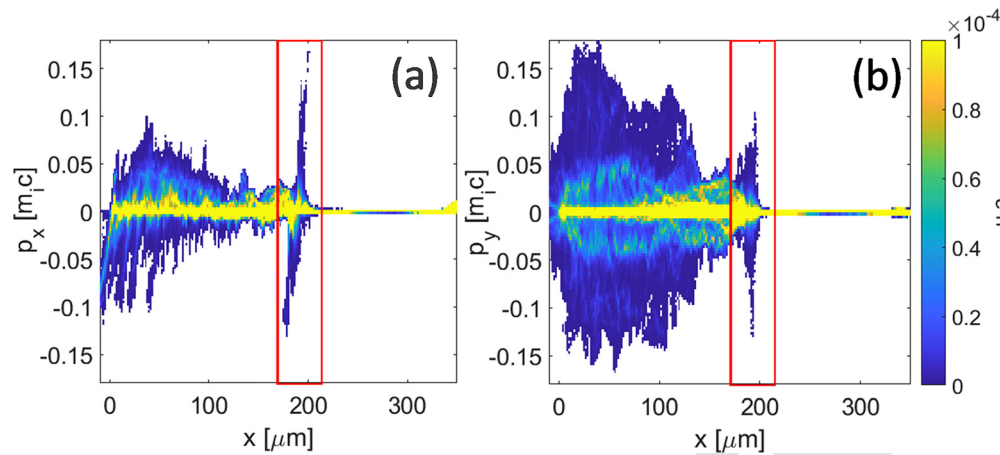


FIG. 12. Proton phase space histogram at time $t = 1.8$ ps: (a) longitudinal and (b) transverse momenta as a function of the longitudinal coordinate.

297 Isotropic acceleration with an average flux of 10^{11} protons/MeV/sr in
 298 the energy range of up to 1.5 MeV, observed in the experiment, is well
 299 reproduced in the PIC simulation. The energy range is higher than in the
 300 experiment, which can be explained by the fact that proton energies can be
 301 overestimated in 2D simulations.³⁴ This broad angle acceleration is present
 302 because the laser interacts first with a smooth plasma density profile. Its
 303 maximum energy depends on the length of the laser path before collapse.

304 We also succeeded to identify the collisionless shock produced
 305 in the hole boring process as the origin of the plateau in the proton
 306 energy distribution at near forward directions. The energy range of
 307 the plateau and the direction of the proton propagation depend on
 308 the initial conditions: the characteristics of the laser pulse and the
 309 ASE level. It was observed that the initial shock direction was the longi-
 310 tudinal one. However, the deviation of the laser beam affects the
 311 angular distribution of the energy plateau at longer times. In particu-
 312 lar, it is influenced by the laser self-focusing in the underdense
 313 plasma. The subsequent filaments of the laser beam interact sepa-
 314 rately with the steepest part of the density profile producing their
 315 deflection. In the experiment, the laser interacts with the gas before

$x = 0$ due to the smooth border of the gas profile. This means that the
 laser may not, in fact, focus at the simulated focal point and the curva-
 ture of its trajectory can be different from the simulated one. It is
 highly probable that the laser beam bends to higher angles inducing a
 plateau structure in the transverse direction as seen in the experiment.
 Concerning the ASE level, the worst contrast may generate a less steep
 density slope at $x = 185 \mu\text{m}$, leading to smaller plateau structures.

A striking feature of the experimental energy spectra is the
 peaked structures. They are measured at different angles depending on
 the laser shot. In the simulation spectrum shown in Fig. 17, a high-
 energy particle bunch separated from the principal structure is also
 observed at 12 MeV in the 23° direction. These types of features are
 highly dependent on the initial parameters of the simulation and, in
 this case, are not predicted at the angles where the parabolas were
 placed in the experiment.

V. CONCLUSION

In our experiment, proton acceleration is observed at 0° , 30° ,
 70° , and 80° using a supersonic H_2 gas-jet target. An isotropic

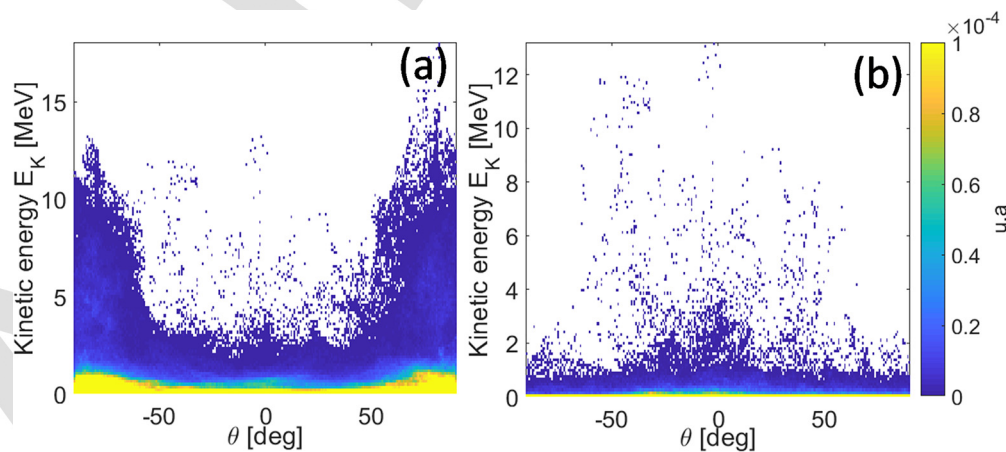


FIG. 13. Angular energy distribution of (a) all forward-accelerated protons and (b) forward protons accelerated between $x = 185 \mu\text{m}$ and $x = 210 \mu\text{m}$ at $t = 1.8$ ps.

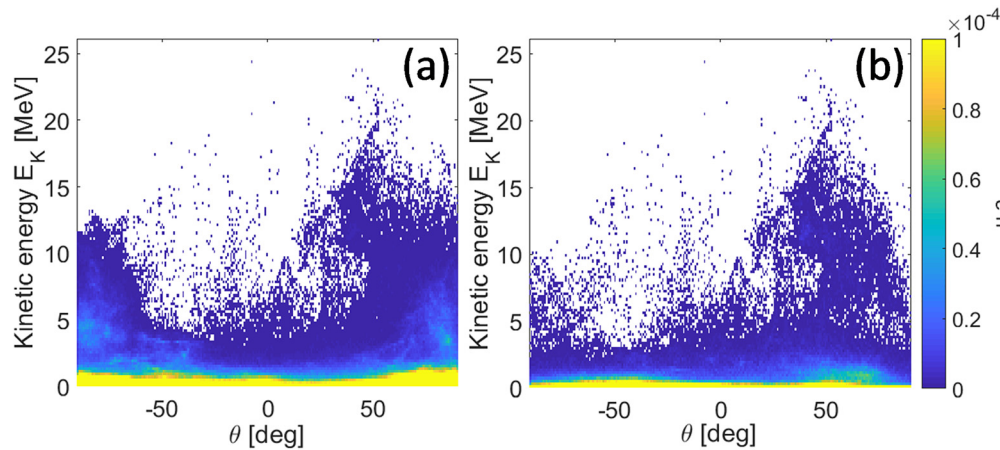


FIG. 14. Angular energy distribution of (a) all forward-accelerated protons and (b) forward shock protons accelerated in the interval $x = 185 \mu\text{m}$ to $x = 250 \mu\text{m}$ at $t = 2.3$ ps.

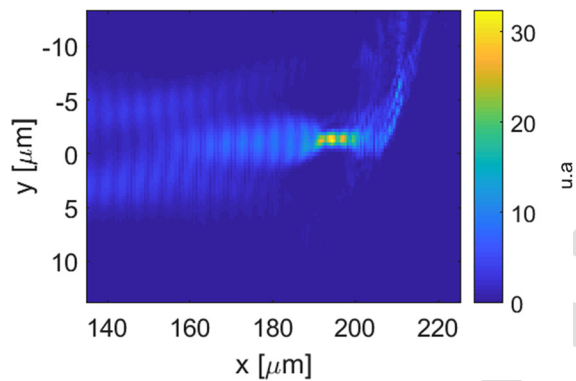


FIG. 15. Period-averaged electromagnetic laser energy $E_z^2 + E_y^2 + (cB_z)^2$ at 2.3 ps.

acceleration with a flux of 10^{11} protons/MeV/sr is measured at low energies of up to 1.5 MeV. Furthermore, a second structure with a constant flux of particles (plateau) is observed in the transverse directions, sometimes even at 30° (Fig. 5). During the experiment, we have verified the advantage of focusing the laser at the rising slope of the gas density profile and of the use of a cleaner pulse by reducing the ASE level. In the best conditions, a maximum energy of 6 MeV was observed in the longitudinal direction. Energy spectra were successfully explained using plasma hydrodynamics and the PIC simulation codes. Self-focusing and self-channeling of the laser beam were observed in the underdense part of the plasma. It is responsible for the transverse acceleration reported. Moreover, a dramatic change of the density profile, produced by the reduction of the ASE level, induces a collisionless shock during the hole boring process. This shock accelerates protons to higher energies creating plateau structures in the spectra. Energetic peaked structures are observed at different angles in several shots which were also found in the simulations.

To our knowledge, these are the first significant high-energy proton spectra from the proton acceleration experiments when high-power infrared lasers interact with the supersonic gas-jet targets. As

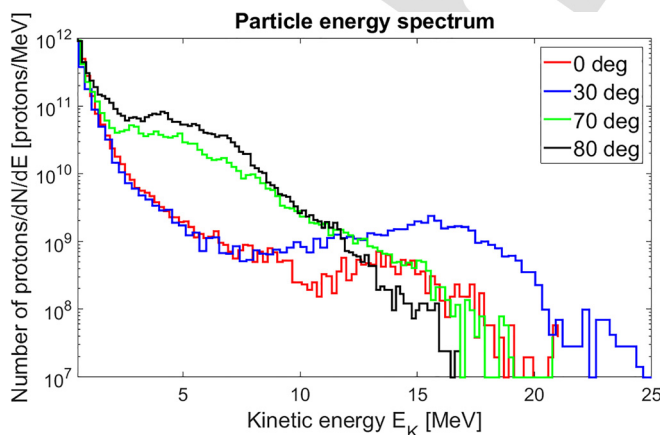


FIG. 16. Forward proton energy distribution at 3.6 ps from the PIC simulations. A 10° wide angular window was taken for each spectrum.

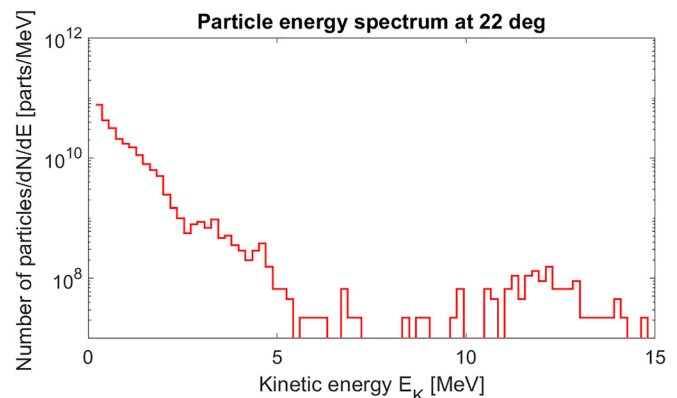


FIG. 17. Forward proton energy distribution at 3.6 ps from the PIC simulations from 21° to 23° .

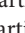


354 explained above, a less than 1 MeV proton energy was reported in
355 Refs. 19 and 20.

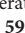
356 In the future, we want to improve the gas-jet density profile in
357 order to enhance the collisionless shock acceleration in the longitudinal
358 direction with respect to other processes. This will be achieved by
359 designing new nozzles and adding optical shaping of the plasma
360 target.³⁵

362 **ACKNOWLEDGMENTS**

363 The authors would like to thank the staff of the LULI facility
364 and the CENBG technical departments for the technical assistance
365 during the experiment, in particular, Edouard Veuillot for his
366 permanent help, Mathieu Chevrot for his outstanding involvement
367 during the experiment, Simon Vallières for his help with the PIC
368 simulations, and Laurent Gremillet for enlightening discussions.
369 This work is supported by Nos. ANR-17-CE30-0026-02, POPRA,
370 and IN2P3-CNRS 2016-2020 (ALP-IONS projects) grants; M.E.
371 and J.J.S. acknowledge the financial support from the Programme
372 IdEx Bordeaux—LAPHIA (No. ANR-10-IDEX-03-02). PIC
373 simulations are possible with the use of High Performance
374 Computing resources of Compute Canada (Job: pve-323-ac, P.
375 Antici). The FLASH software used was developed, in part, by the
376 DOE NNSA ASC- and the DOE Office of Science ASCR-supported
377 Flash Center for Computational Science at the University of
378 Chicago.

379 **REFERENCES**

380 ¹H. Daido, M. Nishiuchi, and A. S. Pirozhkov, "Review of laser-driven ion sources
381 and their applications," *Rep. Prog. Phys.* **75**, 056401 (2012).
382 ²L. Pommarel, B. Vauzour, F. Mégnin-Chanet, E. Bayart, O. Delmas, F. Goudjil,
383 C. Nauraye, V. Letellier, F. Pouzoulet, F. Schillaci, F. Romano, V. Scuderi, G.
384 A. P. Cirrone, E. Deutsch, A. Flacco, and V. Malka, "Spectral and spatial shap-
385 ing of a laser-produced ion beam for radiation-biology experiments," *Phys.*
386 *Rev. Accel. Beams* **20**, 032801 (2017).
387 ³See <http://www.apollon-laser.fr/> for .
388 ⁴See <https://eli-laser.eu/> for .
389 ⁵See <https://www.clpu.es/> for .
390 ⁶D. Margarone, A. Velyhan, J. Dostal, J. Ullschmied, J. P. Perin, D. Chatain, S.
391 Garcia, P. Bonnay, T. Pisarczyk, R. Dudzak, M. Rosinski, J. Krasa, L. Giuffrida,
392 J. Prokupek, V. Scuderi, J. Psikal, M. Kucharik, M. De Marco, J. Cikhhardt, E.
393 Krousky, Z. Kalinowska, T. Chodukowski, G. A. P. Cirrone, and G. Korn,
394 "Proton acceleration driven by a nanosecond laser from a cryogenic thin solid-
395 hydrogen ribbon," *Phys. Rev. X* **6**, 041030 (2016).
396 ⁷L. Obst, S. Göde, M. Rehwald, F.-E. Brack, J. Branco, S. Bock, M. Bussmann, T.
397 E. Cowan, C. B. Curry, F. Fiuza, M. Gauthier, R. Gebhardt, U. Helbig, A.
398 Huebl, U. Hübner, A. Irman, L. Kazak, J. B. Kim, T. Kluge, S. Kraft, M. Loeser,
399 J. Metzkes, R. Mishra, C. Rödel, H.-P. Schlenvoigt, M. Siebold, J.
400 Tiggesbäumker, S. Wolter, T. Ziegler, U. Schramm, S. H. Glenzer, and K. Zeil,
401 "Efficient laser-driven proton acceleration from cylindrical and planar cryo-
402 genic hydrogen jets," *Sci. Rep.* **10**, 1038 (2017).
403 ⁸A. Macchi, M. Borghesi, and M. Passoni, "Ion acceleration by superintense
404 laser-plasma interaction," *Rev. Mod. Phys.* **85**, 751–793 (2013); and references
405 therein.
406 ⁹S. Karsch, S. Düsterer, H. Schwoerer, F. Ewald, D. Habs, M. Hegelich, G.
407 Pretzler, A. Pukhov, K. Witte, and R. Sauerbrey, "High-intensity laser induced
408 ion acceleration from heavy-water droplets," *Phys. Rev. Lett.* **91**, 015001
409 (2003).
410 ¹⁰S. Ter-Avetisyan, M. Schnürer, S. Busch, E. Risse, P. V. Nickles, and W.
411 Sandner, "Spectral dips in ion emission emerging from ultrashort laser-driven
412 plasmas," *Phys. Rev. Lett.* **93**, 155006 (2004).


¹¹M. Schnürer, S. Ter-Avetisyan, S. Busch, E. Risse, M. P. Kalachnikov, W. 413
Sandner, and P. V. Nickles, "Ion acceleration with ultrafast laser driven water 414
droplets," *Laser Part. Beams* **23**, 337–343 (2005). 415
¹²P. Hilz, T. M. Ostermayr, A. Huebl, V. Bagnoud, B. Borm, M. Bussmann, M. 416
Gallei, J. Gebhard, D. Haffa, J. Hartmann, T. Kluge, F. H. Lindner, P. Neumayr, 417
C. G. Schaefer, U. Schramm, P. G. Thirolf, T. F. Röscher, F. Wagner, B. Zielbauer, 418
and J. Schreiber, "Isolated proton bunch acceleration by a petawatt laser pulse," 419
Nat. Commun. **9**, 1 (2018). 420
¹³P. L. Poole, C. D. Andereck, D. W. Schumacher, R. L. Daskalova, S. Feister, K. 421
M. George, C. Willis, K. U. Akli, and E. A. Chowdhury, "Liquid crystal films as 422
on-demand, variable thickness (50–5000 nm) targets for intense lasers," *Phys.* 423
Plasmas **21**, 063109 (2014). 424
¹⁴L. Silva, M. Marti, J. R. Davies, and R. A. Fonseca, "Proton shock acceleration 425
in laser-plasma interactions," *Phys. Rev. Lett.* **92**, 015002 (2004). 426
¹⁵E. d'Humières, J. L. Feugeas, P. Nicolai, S. Gaillard, T. Cowan, Y. Sentoku, and 427
V. Tikhonchuk, "Investigation of high intensity laser proton acceleration with 428
underdense targets," *J. Phys.* **244**, 042023 (2010). 429
¹⁶D. Harberberger, S. Tochitsky, F. Fiuza, C. Gong, R. A. Fonseca, L. O. Silva, W. 430
B. Mori, and C. Joshi, "Collisionless shocks in laser-produced plasma generate 431
monoenergetic high-energy proton beams," *Nat. Phys.* **8**, 95–99 (2012). 432
¹⁷C. Palmer, N. P. Dover, I. Pogorelsky, M. Babzien, G. I. Dudnikova, M. 433
Ispiriyan, M. N. Polyanskiy, J. Schreiber, P. Shkolnikov, V. Yakimenko, and Z. 434
Najmudin, "Monoenergetic proton beams accelerated by a radiation pressure 435
driven shock," *Phys. Rev. Lett.* **106**, 014801 (2011). 436
¹⁸M. H. Helle, D. F. Gordon, D. Kaganovich, Y. Chen, J. P. Palastro, and A. Ting, 437
"Laser-accelerated ions from a shock-compressed gas foil," *Phys. Rev. Lett.* **117**, 438
165001 (2016). 439
¹⁹F. Sylla, A. Flacco, S. Kahaly, M. Veltcheva, A. Lifschitz, V. Malka, E. 440
d'Humières, I. Andriyash, and V. Tikhonchuk, "Short intense laser pulse col- 441
lapse in near-critical plasma," *Phys. Rev. Lett.* **110**, 085001 (2013). 442
²⁰S. N. Chen, M. Vranic, T. Gangolf, E. Boella, P. Antici, M. Bailly-Grandvaux, 443
P. Loiseau, H. Pépin, G. Revet, J. J. Santos, A. M. Schroer, M. Starodubtsev, O. 444
Willi, L. O. Silva, E. d'Humières, and J. Fuchs, "Collimated protons accelerated 445
from an overdense gas jet irradiated by a 1 mm wavelength high-intensity 446
short-pulse laser," *Sci. Rep.* **7**, 13505 (2017). 447
²¹J. L. Henaes, T. Tarisien, P. Puyuelo, J.-R. Marquès, T. Nguyen-Bui, F. Gobet, 448
X. Raymond, M. Versteegen, and F. Hannachi, "Optimization of critical- 449
density gas jet targets for laser ion acceleration in the collisionless shockwave 450
acceleration regime," *J. Phys.* **1079**, 012004 (2018). 451
²²J. L. Henaes, P. Puyuelo-Valdes, F. Hannachi, T. Ceccotti, M. Ehret, F. Gobet, 452
L. Lancia, J.-R. Marquès, J. J. Santos, M. Versteegen, and M. Tarisien, 453
"Development of critical-density gas jet targets for laser-driven ion accel- 454
eration," *Rev. Sci. Instrum.* **90**, 063302 (2019). 455
²³T. Bonnet, M. Comet, D. Denis-Petit, F. Gobet, F. Hannachi, M. Tarisien, M. 456
Versteegen, and M. M. Leonard, "Response functions of Fuji imaging plates to 457
monoenergetic protons in the energy range 0.6–3.2 MeV," *Rev. Sci. Instrum.* 458
84, 013508 (2013). 459
²⁴See <http://www.cenbg.in2p3.fr/-Plateforme-AIFIRA-> for .
460
²⁵Y. Sentoku and A. J. Kemp, "Numerical methods for particle simulations at 461
extreme densities and temperatures: Weighted particles, relativistic collisions 462
and reduced currents," *J. Comput. Phys.* **227**(14), 6846–6861 (2008). 463
²⁶B. Fryxell, K. Olson, P. Ricker, F. X. Timmes, M. Zingale, D. Q. Lamb, P. 464
MacNeice, R. Rosner, and H. Tufo, "FLASH: An adaptivemesh hydrodynamics 465
code for modelling astrophysical thermonuclearflashes," *Astrophys. J. Suppl.* 466
Ser. **131**, 273–334 (2000). 467
²⁷K. Krushelnick, E. L. Clark, Z. Najmudin, M. Salvati, M. I. K. Santala, M. 468
Tatarakis, and A. E. Dangor, "Multi-MeV ion production from high-intensity 469
laser interactions with underdense plasmas," *Phys. Rev. Lett.* **83**, 737 (1999). 470
²⁸G. S. Sarkisov, V. Y. Bychenkov, V. N. Novikov, V. T. Tikhonchuk, A. 471
Maksimchuk, S.-Y. Chen, R. Wagner, G. Mourou, and D. Umstadter, "Self- 472
focusing, channel formation, and high-energy ion generation in interaction of 473
an intense short laser pulse with a He jet," *Phys. Rev. E* **59**, 7042 (1999). 474
²⁹M. S. Wei, S. P. D. Mangles, Z. Najmudin, B. Walton, A. Gopal, M. Tatarakis, 475
A. E. Dangor, E. L. Clark, R. G. Evans, S. Fritzler, R. J. Clarke, C. Hernandez- 476
Gomez, D. Neely, W. Mori, M. Tzoufras, and K. Krushelnick, "Ion acceleration 477
by collisionless shocks in high-intensity-laser-underdense-plasma interaction," 478
Phys. Rev. Lett. **93**, 155003 (2004). 479

AQ4

AQ5

AQ3

AQ7

- 480 ³⁰L. Willingale, S. P. D. Mangles, P. M. Nilson, R. J. Clarke, A. E. Dangor, M. C.
481 Kaluza, S. Karsch, K. L. Lancaster, W. B. Mori, Z. Najmudin, J. Schreiber, A. G.
482 R. Thomas, M. S. Wei, and K. Krushelnick, "Collimated multi-MeV ion beams
483 from high-intensity laser interactions with underdense plasma," *Phys. Rev.*
484 *Lett.* **96**, 245002 (2006).
- 485 ³¹P. Puyuelo-Valdes, J.-L. Henares, F. Hannachi, T. Ceccotti, J. Domange, M. Ehret,
486 E. D'Humieres, L. Lancia, J.-R. Marquès, J. Santos, and M. Tarisien, "Laser driven
487 ion acceleration in high-density gas jets," *Proc. SPIE* **11037**, 110370B (2019).
- 488 ³²S. C. Wilks, W. L. Kruer, M. Tabak, and A. B. Langdon, "Absorption of
489 intense laser pulses," *Phys. Rev. Lett.* **69**, 1383 (1992). 
- ³³V. Mironov, N. Zharova, E. d'Humieres, R. Capdessus, and V. T. Tikhonchuk, 490
491 "Effect of the laser pulse temporal shape on the hole boring efficiency," *Plasma*
492 *Phys. Controlled Fusion* **54**, 095008 (2012).
- ³⁴C. S. Brady and T. D. Arber, "An ion acceleration mechanism in laser illumi- 493
494 nated targets with internal electron density structure," *Plasma Phys. Controlled*
495 *Fusion* **53**, 015001 (2011).
- ³⁵O. Tresca, N. P. Dover, N. Cook, C. Maharjan, M. N. Polyanskiy, Z. Najmudin, 496
497 P. Shkolnikov, and I. Pogorelsky, "Spectral modification of shock accelerated
498 ions using a hydrodynamically shaped gas target," *Phys. Rev. Lett.* **115**, 094802
499 (2015).